PHYSICAL REVIEW A VOLUME 52, NUMBER 3 SEPTEMBER 1995

Optical-rotation technique used for a high-precision measurement of parity nonconservation in atomic lead

D. M. Meekhof,* P. A. Vetter, P. K. Majumder,† S. K. Lamoreaux, and E. N. Fortson
Department of Physics, FM-15, University of Washington, Seattle, Washington 98195

(Received 13 March 1995)

We have measured the parity-nonconserving (PNC) optical rotation near the 1.279-μm ${}^3P_0 \rightarrow {}^3P_1$ magnetic-dipole absorption line in atomic lead vapor. We measure the quantity $\mathcal{R} \equiv \text{Im}\,(\mathcal{E}_{\text{PNC}}/\mathcal{M})$, where $\mathcal{M}$ is the magnetic-dipole amplitude of the absorption line and $\mathcal{E}_{\text{PNC}}$ is the electric-dipole amplitude coupled into the same line by the PNC interaction within the lead atom. We find $\mathcal{R}$ to be $(-9.86 \pm 0.04 \pm 0.11) \times 10^{-8}$, where the first error is statistical and the second is systematic. The statistical errors are due to incompletely subtracted background fluctuations, and the systematic errors are caused by line-shape uncertainties and calibration error. Our value is consistent with the atomic PNC calculations for lead, which give $\mathcal{R} = (-10.7 \pm 0.8) \times 10^{-8}$ for the standard electroweak model with $\sin^2\theta_W = 0.23$ and no electroweak radiative corrections. Including radiative corrections yields the value $S = -3 \pm 8$ for the isospin-conserving electroweak parameter, with difficulties in the atomic theory of lead presently limiting the extent to which our result tests the standard model. This same technique can also be applied to thallium, where the atomic theory is currently accurate to 3%. By searching for a difference in $\mathcal{R}$ for the two hyperfine components of ^{207}Pb, we find the amplitude of the nuclear spin-dependent PNC rotation to be less than 2×10^{-2} of the nuclear spin-independent rotation.

PACS number(s): 32.80.Ys, 11.30.Er

I. INTRODUCTION

The standard model of electroweak interactions predicts parity nonconservation (PNC) in atoms caused by the exchange of the neutral Z_0 boson between atomic electrons and quarks in the nucleus [1]. High-precision atomic PNC experiments, coupled with precise atomic theory in the atoms under study, can test the heavy physics of and unknown physics beyond the standard model. These measurements have certain unique features [2]; they are sensitive only to the isospin-conserving class of corrections to the standard model and to the possible existence of a second Z_0 boson. PNC has been measured in a number of heavy elements [3]. Thus far, Cs PNC has provided the best atomic probe of electroweak physics because the effects of atomic structure in this element have been calculated to an accuracy of 1% [4] and the measurement of cesium PNC has reached 2% [5].

We reported in Ref. [6] a 1.2% measurement of parity-nonconserving optical rotation on the 1.28-μm magnetic-dipole absorption line in lead vapor, the most accurate atomic PNC measurement to date. Here we present a detailed description of the experimental apparatus, the measurement technique, and the line-shape and systematics analysis. This technique lays the foundation for new atomic tests of the standard model. For example, an experiment with the same apparatus has been carried out quite recently on thallium [7], using a magnetic-dipole line at nearly the identical wavelength as lead for which the size of PNC can be calculated much more reliably. With the current accuracy of 3% in thallium theory [8], this measurement tests the standard model at the same level as cesium and improved calculations are expected [9]. Another possible use of this technique is the measurement of PNC on a string of separated lead isotopes to cancel the uncertain effects of atomic structure [10,11].

All measurements of PNC by optical rotation are based on the interference between $\mathcal{M}$, the allowed magnetic-dipole amplitude between two nominally same-parity states of an atom, and $\mathcal{E}_{\text{PNC}}$, the electric-dipole amplitude coupled into the same line by the PNC interaction within the atom. The measured quantity is the ratio $\mathcal{R} \equiv \text{Im}\,(\mathcal{E}_{\text{PNC}}/\mathcal{M})$. Such measurements have a long history in our laboratory. The present apparatus incorporates extensive revisions, including a spectrally sharper laser source, much improved subtraction of background rotations, improved calibration, and more efficient line-shape analysis.

In Sec. II of this paper we discuss atomic parity nonconservation as predicted by the standard model, in Sec. III the genesis of observable optical rotation by atomic PNC, and in Sec. IV the general method of measuring optical rotation and the specific improvements made in this experiment. In Sec. V we describe the apparatus in detail, in Sec. VI the method of data acquisition, in Sec. VII the fitting programs for the analysis of the many data traces, in Sec. VIII the angle calibration and error analysis, and in Sec. IX we discuss the significance of the results and point out future directions.

---

*Present address: Time and Frequency Division, National Institute of Standards and Technology, Boulder, CO 80303.

†Present address: Department of Physics, Williams College, Williamstown, MA 01267.

1050-2947/95/52(3)/1895(14)/$06.00

II. ELECTROWEAK INTERACTION IN ATOMS

The main source of atomic PNC is the exchange of the Z_0 boson between electrons and nucleons. Because of the large Z_0 mass ($\cong$ 90 GeV) the Hamiltonian is a contact interaction summed over the atomic electrons and nucleons and in the limit of nonrelativistic nucleons becomes [12]:

$$\mathcal{H}_{\text{PNC}} = \frac{G_f}{\sqrt{2}} \sum_{e,\mathcal{N}} \left[C_{1\mathcal{N}} \int \psi_{\mathcal{N}}^{\dagger} \psi_{\mathcal{N}} \psi_e^{\dagger} \gamma^5 \psi_e \, d^3r \right. \quad (1)$$
$$\left. + C_{2\mathcal{N}} \int \psi_{\mathcal{N}}^{\dagger} \boldsymbol{\sigma}_{\mathcal{N}} \psi_{\mathcal{N}} \cdot \psi_e^{\dagger} \boldsymbol{\alpha} \psi_e \, d^3r \right] .$$

The coupling coefficients, as given by the standard model at tree level, are [13]

$$\begin{aligned} C_{1p} &= \frac{1}{2}(1 - 4\sin^2\theta_W) \sim 0.04, \\ C_{1n} &= -\frac{1}{2} = -0.5, \\ C_{2p} &= \frac{1}{2}(1 - 4\sin^2\theta_W) g_A \sim -0.05, \\ C_{2n} &= -\frac{1}{2}(1 - 4\sin^2\theta_W) g_A \sim 0.05, \end{aligned}$$

where $\sin^2\theta_W = 0.23$, in lowest order, and $g_A = 1.25$ is the ratio between the vector and axial vector coupling constants as measured in neutron β decay.

The C_1 terms in Eq. (1) are independent of nuclear spin and sum coherently over all the nucleons to yield the spin-independent (SI) PNC Hamiltonian for each electron

$$\mathcal{H}_{\text{SI}} = \frac{G_F}{\sqrt{2}} \frac{Q_W}{2} \int \rho_{\mathcal{N}}(r) \psi_e^{\dagger} \gamma^5 \psi_e \, d^3r , \quad (2)$$

where $\rho_{\mathcal{N}}(r)$ is the nuclear density normalized to unity and Q_W is known as the weak charge. In the Standard Model, omitting radiative corrections,

$$\begin{aligned} Q_W &= 2(ZC_{1p} + NC_{1n}) & (3) \\ &= -N + Z(1 - 4\sin^2\theta_W) & (4) \end{aligned}$$

for a nucleus of Z protons and N neutrons.

Q_W is the quantity of interest for comparison with fundamental electroweak theory. Radiative corrections within the standard model produce corrections to Q_W at the several percent level [2]. Corrections due to heavy physics (Higgs boson and top quark) and to possible unknown particles can be divided into isospin-conserving and isospin-breaking components, labeled S and T, respectively. Including these radiative corrections yields, to a good approximation,

$$\begin{aligned} Q_W = {} & (0.9857 \pm 0.0004)(1 + 0.00782T) \\ & \{-N + Z[1 - (4.012 \pm 0.010)\bar{x}]\} \\ & + Q_{\text{tree}}^{\text{new}}(N, Z), \end{aligned} \quad (5)$$

where $\bar{x} \equiv \sin^2\theta_W$ is defined at the mass scale M_Z and is given by

$$\bar{x} = 0.2323 \pm 0.0007 + 0.00365S - 0.00261T. \quad (6)$$

S and T are defined as in [2] and the final term in Eq. (5) accounts for possible new tree-level physics such as a second Z_0 boson. Atomic PNC is unique among electroweak physics tests in that the T dependence in Q_W, including that in $\bar{x}$, cancels nearly completely for values of Z/N characteristic of heavy atoms [2].

The C_2 terms in Eq. (1) are nuclear spin-dependent (SD) and sum to no more than a small fraction ($\approx 1/Q_W$) of the spin-independent effect since only the unpaired nuclear spins make a net contribution. The SD Hamiltonian for each electron may be written

$$\mathcal{H}_{\text{SD}} = \frac{G_F}{\sqrt{2}} \frac{\kappa_a}{2} \mathbf{I} \cdot \int \rho_{\mathcal{N}}(r) \psi_e^{\dagger} \boldsymbol{\alpha} \psi_e d^3r , \quad (7)$$

where $\mathbf{I}$ is the spin of the nucleus and κ_a includes not only the C_2 terms, which are small because $\sin^2\theta_W$ is close to 0.25, but also the somewhat larger contribution expected from the nuclear anapole moment [14]. The anapole moment, which arises from PNC interactions within the nucleus, couples electromagnetically to the electrons to produce the same form of atomic Hamiltonian as the C_2 terms. It is important to note that any SD contribution will yield zero if summed over all of the hyperfine components of a transition.

III. OBSERVABLE PNC EFFECTS

The PNC Hamiltonian can mix a small amplitude of opposite-parity wave function into an atomic state. The electric-dipole matrix element induced between nominally identical parity states $|i\rangle$ and $|f\rangle$ is given by

$$\begin{aligned} \mathcal{E}_{\text{PNC}} &= \langle f' | \mathbf{D} | i' \rangle \\ &= \sum_m \left[\frac{\langle f | \mathcal{H}_{\text{PNC}} | m \rangle \langle m | \mathbf{D} | i \rangle}{E_f - E_m} \right. \\ &\qquad \left. + \frac{\langle f | \mathbf{D} | m \rangle \langle m | \mathcal{H}_{\text{PNC}} | i \rangle}{E_i - E_m} \right], \end{aligned}$$

where $\mathbf{D} = \sum_k e\mathbf{r}_k$ is the electric-dipole operator for the electrons and $|m\rangle$ and E_m denote the unperturbed wave functions and energies. The size of $|\boldsymbol{\mathcal{E}}_{\text{PNC}}|$ increases approximately as Z^3 [1] and for heavy atoms, such as lead and thallium, is of order $10^{-9} ea_0$. $\mathcal{E}_{\text{PNC}}$ can be measured through interference between the electric- and magnetic-dipole amplitudes of the $i \to f$ transition, with the magnetic-dipole matrix element between the same states given by

$$\boldsymbol{\mathcal{M}} = -\frac{e\hbar}{2m_e c} \langle f | \mathbf{L} + 2\mathbf{S} | i \rangle .$$

Generally, $\mathcal{E}_{\text{PNC}} \ll \mathcal{M}$.

If a circularly polarized electromagnetic wave is introduced, the transition probability is proportional to

$$|\boldsymbol{\mathcal{M}} \cdot \mathbf{B}_\eta + \boldsymbol{\mathcal{E}}_{\text{PNC}} \cdot \mathbf{E}_\eta|^2 ,$$

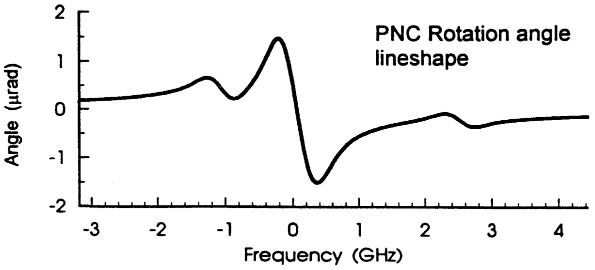

FIG. 1. Theoretical PNC rotation line shape at the 1.28-μm line in Pb at 30 absorption depths of vapor.

where $\mathbf{E}_\eta, \mathbf{B}_\eta$ are electric- and magnetic-field components with $\eta = \pm$ helicity. The fractional difference in transition probability, and hence in the absorption of the wave, is

$$\frac{\kappa_+ - \kappa_-}{\kappa} = 2\mathrm{Im}\left(\frac{\mathcal{E}_{\mathrm{PNC}}}{\mathcal{M}}\right) \equiv 2\mathcal{R} = -\frac{n_+ - n_-}{2(n-1)},$$

where κ is the absorptivity of the vapor due to the $M1$ absorption line and n is the associated refractive index. The last equality follows from the Kramers-Kronig relation. The differential index of refraction leads to a phase delay between the different helicity components of a plane polarized light beam upon transmission through the vapor, which creates a rotation of the plane of polarization. The PNC rotation in a length l of vapor is

$$\begin{aligned}\phi_{\mathrm{parity}}(\nu) &= \frac{\pi l}{\lambda}\left[n_+(\nu) - n_-(\nu)\right] \\ &= -\frac{4\pi l}{\lambda}\left[n(\nu) - 1\right]\mathcal{R},\end{aligned} \tag{8}$$

which has the shape of a dispersion curve about the absorption line. The fractional transmission τ of the light beam is

$$\tau(\nu) = e^{-\kappa(\nu)l}. \tag{9}$$

We typically work with lead vapor producing values of κl between 10 and 60 absorption lengths at line center of the $M1$ transition, which creates a PNC rotation of about 10^{-6} rad at the dispersion peaks. The PNC rotation line shape is given by Eq. (A10) and is shown in Fig. 1.

IV. PRINCIPLE OF THE EXPERIMENT

The experimental apparatus is a sensitive polarimeter in which a laser beam passes through two crossed polarizers and, between them, an atomic vapor sample. The transmission and optical rotation of the sample are measured while the laser frequency is swept across the $M1$ absorption line.

The light transmitted by the two crossed polarizers is $\sin^2\phi + \epsilon^2$ with ϕ the angle of rotation between the polarizers and ϵ^2 the transmission at maximum extinction. Typically, $\epsilon^2 \approx 10^{-7}$ in this experiment. To create sensitivity to small signal rotations ϕ_{sig}, an offset angle ϕ_{mod} is introduced, and to discriminate against light intensity fluctuations this angle is modulated by the use of a Faraday glass placed in the optical path after the initial polarizer. The total uncrossing angle is then

$$\phi(\nu) = \phi_{\mathrm{mod}}\cos(\omega t) + \phi_{\mathrm{sig}}(\nu),$$

where the rotations are in general a function of the laser frequency ν. The transmission of the vapor is also a function of the laser frequency, so the light measured at the detector is proportional to

$$\begin{aligned}\tau(\nu)[\phi(\nu)]^2 = \tau[&\tfrac{1}{2}\phi_{\mathrm{mod}}^2\cos(2\omega t) + 2\phi_{\mathrm{sig}}(\nu)\phi_{\mathrm{mod}}\cos(\omega t) \\ &+\phi_{\mathrm{sig}}(\nu)^2 + \tfrac{1}{2}\phi_{\mathrm{mod}}^2 + \epsilon^2],\end{aligned} \tag{10}$$

where we have assumed $\sin^2\phi \approx \phi^2$, an excellent approximation, since in our experiment $\phi_{\mathrm{sig}} \ll \phi_{\mathrm{mod}} \cong 10^{-3}$ rad. Phase-sensitive detection at 2ω extracts a term proportional to τ, for measurement of the transmission function. Detection at 1ω extracts the cross term proportional to $\tau\phi_{\mathrm{sig}}$. This rotation signal consists of the PNC angle of interest plus two other rotation patterns

$$\phi_{\mathrm{sig}}(\nu) = \phi_{\mathrm{parity}}(\nu) + \phi_{\mathrm{Faraday}}(\nu) + \phi_{\mathrm{back}}(\nu), \tag{11}$$

with $\phi_{\mathrm{Faraday}}(\nu)$ the Faraday rotation of the lead vapor at the 1.28-μm absorption line when a magnetic field is present and $\phi_{\mathrm{back}}(\nu)$ the background rotation due to imperfections in the windows and polarizers.

The Faraday effect is a parity-conserving optical rotation produced by a magnetic field parallel to the direction of propagation of the light [12]. The magnetic field splits the atomic sublevels, shifting the line center of transitions with $\Delta m = \pm 1$ and also mixes hyperfine sublevels. The optical rotation due to the sublevel splitting has a line shape proportional to the derivative of a dispersion shape, while the smaller part due to the state mixing has just the dispersion shape about each hyperfine component of the absorption line. Thus $\phi_{\mathrm{Faraday}}(\nu)$ is a well understood function of the atomic line-shape parameters, such as the line strengths, isotope shifts and abundances, and the Doppler and Lorentz widths. The theoretical Faraday rotation line shape is given by Eq. (A13) and displayed in Fig. 2. Higher-order rotation effects that are quadratic in the magnetic-field strength and contain dependence on off-axis field components are not included because they are negligible under the conditions of this experiment and are further suppressed by the averaging over polarizer orientations that is done in the course of the measurements.

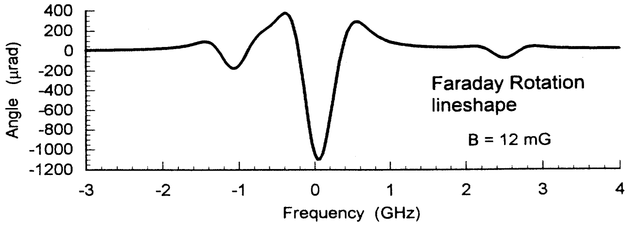

FIG. 2. Theoretical Faraday rotation line shape at the 1.28-μm line in Pb at 30 absorption depths of vapor and 15 mG magnetic field.

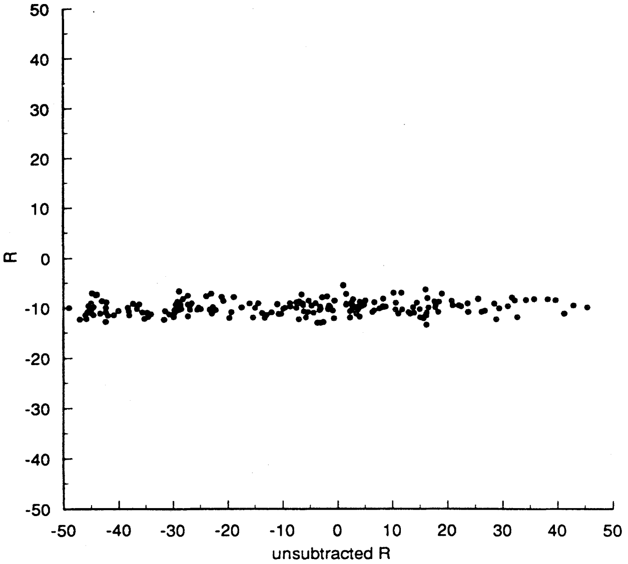

FIG. 3. Scatter plot of $\mathcal{R}$ vs $\mathcal{R}_{\rm unsub}$. $\mathcal{R}_{\rm unsub}$ is the measured value of $\mathcal{R}$ found from the same data, analyzed without the $\phi_{\rm back}$ removal. The bounds of the graph are made equal to display the efficacy of the background subtraction technique. For these data $\mathcal{R}_{\rm unsub} = -9.80 \pm 0.42$ and $\mathcal{R} = -9.87 \pm 0.03$.

For the absolute angle calibration of the signal, we found that using the magnitude of $\phi_{\rm Faraday}(\nu)$ provides a more reliable calibration than using mechanical rotations. A precisely known magnetic field on the vapor sample is needed and it is provided by a coil wound around the lead sample tube. A mechanical calibration is also carried out to provide a useful check of the calculation of the Faraday line shape and to study variations in the apparatus's sensitivity with changes in optical elements.

A major improvement in the current experiment has been the method chosen for dealing with the spurious wavelength-dependent optical rotations $\phi_{\rm back}(\nu)$ that occur even in the absence of the atomic vapor between the polarizer and analyzer. Birefringences and multiple paths of the light due to scattering in the optical elements between (and including) the two polarizers cause these background rotations. Since the PNC signal is roughly the same size, these rotations present a serious problem. The oven for heating the lead vapor sample is designed to permit moving the lead vapor into and out of the optical path. In this way, we can measure the rotation due solely to the optical elements and subtract the background rotation effects from the data. A scatter plot of the value of $\mathcal{R}$ found with and without background subtraction, given in Fig. 3, clearly displays the importance of this correction.

V. DETAILS OF THE EXPERIMENTAL APPARATUS

A schematic diagram of the entire experiment is shown in Fig. 4. We discuss each part of the apparatus in order along the optical path.

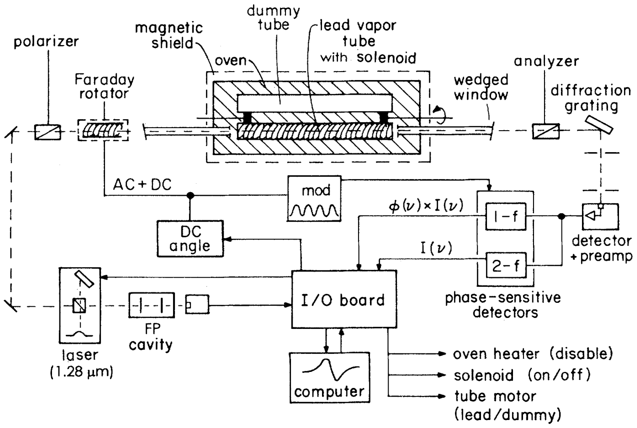

FIG. 4. Block diagram of the experiment.

A. 1.3-μm laser

For high precision spectroscopic measurements a laser is needed that has very high spectral purity and is continuously tunable over the entire atomic line shape. Recent improvements in the availability, power output, and wavelength coverage of diode lasers has made a significant impact on atomic laser spectroscopy. Diode lasers do not put out a large amount of power, but for our type of application this is only a consideration when photon shot noise is a dominate source of experimental uncertainty. The most convenient way to attain spectral purity and wavelength control with commercially available diode lasers is to use optical feedback by coupling the laser diode cavity into an external cavity.

In a standard diode laser, the lasing medium itself has a fairly broad gain spectrum, typically a few tens of nanometers. The cavity modes of the diode are typically separated by a nanometer and have a width on the order of 100 MHz. Since this separation is usually smaller than the range of intrinsic gain of the medium, the diode will lase simultaneously in several cavity modes. Some single-mode diode lasers are manufactured and these can be frequency tuned by varying the temperature on the diode. Temperature tuning of the laser is a result of the combined effect of tuning of the gain medium and tuning of the diode cavity. Unfortunately, the coefficient of central gain wavelength vs temperature for these two mechanisms is quite different, so there will be frequent longitudinal cavity mode hops while temperature tuning the laser frequency. In addition, temperature tuning the laser is prohibitively slow for rapid data acquisition.

To isolate a single longitudinal cavity mode for lasing, frequency selective optical feedback is used. Feedback using a blazed diffraction grating offers several advantages over other methods, such as use of an intracavity étalon [15].

To increase the laser's susceptibility to the optical feedback the diode can be antireflection coated and the grating arranged to return, typically, over 90% of the light to the laser. The external cavity formed is much longer than the diode's and therefore its gain curve has more closely spaced modes. The modes have a much narrower intrinsic linewidth due to the greatly increased cavity Q. While the fundamental attainable spectral linewidth of the laser is given by the Schawlow-Townes formula, in practice, acoustic pickup and vibrations of the cavity cause a much larger effective linewidth at bandwidths appropriate for our data acquisition rate.

The laser is frequency tuned by changing the angle of the grating feedback. To avoid mode hops, care must be taken to simultaneously adjust the length of the external cavity so that the frequency of the longitudinal cavity mode tracks with the central frequency of the diffraction grating feedback. The mount for the diffraction grating is designed so that a single piezoelectric translation (PZT) element rotates translates the beam spot on the grating in the proper way. Two other PZT's on the grating mount allow precise optimization of the feedback conditions.

Recently, $\mathrm{In}_x\mathrm{Ga}_{1-x}\mathrm{AsP}$ diode lasers covering the $\lambda = 1.2$–1.55 μm frequencies have become available due to their importance for optical communications. As we initially obtained it, the bare diode we used had a center wavelength of about 1310 nm and an output power of 5 mW. Antireflection coating was applied by evaporating a thin film of $\mathrm{Sb_2O_3}$ (n_r=1.86) onto one facet of the diode while monitoring its light output from the opposite facet using the on-chip photodiode. The light output passes through a minimum when the reflection of the output facet is at its lowest. A short focal length lens (6 mm, f-number=0.7) collimates the laser output light. In order to lower the diode from its room temperature wavelength of 1.3 μm, it was housed in a vacuum can along with a Dewar filled with liquid nitrogen. A copper braid connects the liquid nitrogen can to the diode mounting block. Only the diode and the collimating lens are within the vacuum vessel. The collimated laser light exits the can through a window at Brewster's angle. The current to a Peltier heating element is controlled by a feedback loop that senses the block temperature through a thermistor. This maintains the temperature at about $-100\,^\circ$C, shifting the gain curve of the diode down to 1.28 μm. The heater is stable to a few mK. The laser cavity is formed by a diffraction grating 6 cm away from the diode. The grating has 1200 lines/mm blazed for 0.75-μm light and is mounted so that the $m = -1$ order is directed back into the laser. This arrangement is known as the Littrow configuration.

With careful alignment, the voltage ramp to one of the PZT's mounted on the grating assembly can scan the frequency over more than 10 GHz without mode hops. This is more than sufficient for our experiment, since the lead hyperfine splitting is 3.56 GHz. Room vibration, microphonics, and boiling of the liquid nitrogen used for cooling causes cavity vibrations that result in an effective low-frequency linewidth of roughly 5 MHz. The laser produces a 5-mW intracavity of which 0.5 mW is coupled out using a 10% cube beam splitter. About 1% of the laser's output power is off-mode continuum spontaneous emission light, which appears to have a negligible frequency dependence. This is easily accounted for in our line-shape analysis as described in the Appendix.

The low-voltage PZT's used display considerable hysteresis and nonlinearity in response. Therefore, to obtain the laser frequency as a function of the PZT voltage, we detect the light transmitted through a Fabry-Pérot cavity. The free spectral range of the cavity was such that eight peaks are measured in a typical data trace. A simple optical isolator is used to prevent optical feedback to the laser. Before PNC data acquisition, the Fabry-Pérot data are fit as described below and we apply a compensating nonlinear voltage ramp to the PZT's that yields a more linear laser frequency response in the data.

B. Polarizers and Faraday rotator

High-quality polarizers are also crucial for high-precision polarimetry. Imperfections of the surface or within the crystal can scatter the light, allowing multiple optical paths that interfere and contribute to the background rotations. We use two high-quality Glan-Thompson calcite polarizers mounted in specially constructed "angle amplifier mounts" with which we can control the uncrossing angle between the polarizers at the microradian level with ordinary micrometer handles. Nicol-type prism polarizers were used for some of the data and for various tests of the experiment. In general these were found to produce larger background patterns $\phi_{\mathrm{back}}(\nu)$ with more persistent features that did not respond as well to attempts to vary them with optical orientation.

The next element in the optical path after the initial polarizer is the Faraday rotator. The Faraday rotator consists of a glass rod of high Verdet constant in the near infrared, Hoya FR-5, placed within a magnetic field coil. The applied magnetic field rotates the plane of polarization of light passing through the glass. We apply ac at $\omega/2\pi = 1.3$ kHz to the coil in order to modulate the plane of polarization of the laser beam. The rotation for our glass is 65.6 μrad/A. Typically, we modulate with a rotation amplitude of $\phi_{\mathrm{mod}} \sim 10^{-3}$ rad. The size of this amplitude is dictated by optimizing the signal-to-noise ratio. A static current can be applied to a second field coil to provide small optical rotations for mechanical calibration of the apparatus and to null out small, slow, angle drifts during data acquisition.

C. Oven and lead vapor tube

The oven structure consists of two inner ceramic Mullite tubes within the outer Mullite tube, surrounded by clamshell heaters, several layers of insulation, and finally two layers of magnetic shielding. The outer ceramic tube, its water-cooled end caps, and the extensions for the oven windows form the vacuum enclosure. The two inner oven tubes, the lead and the dummy tubes, are mounted in a rotating inner retaining ring to allow the tubes to be exchanged by a 180° rotation. At one end of the oven a shaft extends from this retaining ring through an O-ring seal outside the vacuum and is attached by a gear and chain to a dc motor. The lead and dummy tubes with the mounting rings and shaft form a spindle assembly, which is rotated in 180° steps by the motor to move first one and then the other tube into the optical path.

A 1 m length of the tube is heated to between 850° and 1050 °C to produce a wide range of atomic vapor densities. To confine the lead vapor in the sample tube a buffer gas at 10–30 Torr fills the vacuum enclosure. The ends of the tube extend several inches outside of the heated region. The buffer gas acts to thermalize the lead vapor as it migrates toward the ends of the tube and the cooled vapor condenses onto the wall of the tube without escaping. In this way, no windows are needed on the inner tube to contain the lead vapor and therefore $\phi_{\text{back}}(\nu)$ is left largely unchanged when the lead tube is moved into and out of the optical path. The buffer gas is mostly helium, with some hydrogen added to provide a reducing atmosphere necessary to avoid oxidation of the molybdenum Faraday coil wire or the lead. Generally we used about 1 Torr of hydrogen and 15 Torr of helium. The minimum buffer gas pressure is dictated by the vapor pressure of the lead at a given oven temperature. Typically, the buffer gas pressure was varied somewhat to provide a range of collisional broadening conditions for each data set at a particular oven temperature.

Because the oven windows are in the optical path between the polarizer and the measuring analyzer, it is crucial to minimize their effect on the polarization and amplitude of the light. In early experiments the windows were much closer to the hot area of the oven and it was found that interchanging the lead and dummy tubes disturbed the heating of the windows, producing large drifts in the background rotation signal. In the present design, the oven windows are separated by 30 cm from the hot region of the oven by thin (6-mm-diam) stainless steel tubes and wider flexible bellows, which allow for optical adjustments between data runs without losing vacuum. During data runs, the window mounts are rigidly affixed to the optical platform. To reduce the size of background rotations due to multiple reflections, wedged, antireflection coated windows are used.

We also investigated tilting the oven windows at Brewster's angle and found that the reduced reflection significantly lowers the size of the background rotations. However, the different transmissivity of the windows at Brewster's angle for the incident s and p wave components of the angle-modulated laser light presented a significant problem. This effect changes the angle calibration by roughly 15% as compared to flat or slightly wedged windows. Moreover, the apparatus has a different sensitivity to an optical rotation induced by the Faraday modulator compared to an optical rotation by the atoms since the rotation by the modulator is affected by passage through both Brewster windows, while an optical rotation by the atoms is affected by the exit window only. The calibration is also sensitive to changes in the alignment. Since these changes of alignment are important to diminish the effects of the background rotations and to avoid potential systematic errors, we rejected the use of Brewster's windows. The atomic Faraday calibration corrects for such errors, but an absolute angle calibration is still useful for checking the Faraday calibration and for investigating other systematic effects.

Two layers of cylindrical magnetic shielding surround the oven. The axial shielding factor was measured using a flux-gate magnetometer to be roughly 100. While this factor is somewhat low, our primary concern is with shielding fluctuating axial magnetic fields, so this was considered adequate. Nonaxial fields were measured to be small and to produce a negligible effect on optical rotation.

To produce known magnetic fields on the lead sample for measurements of the Faraday rotation, a coil was wound on the lead vapor tube. The vapor tube was mounted on a lathe and wrapped with four turns per inch of 0.25-mm molybdenum wire, cemented at four places per turn with Al_2O_3 high-temperature cement to prevent the turns from moving either along the tube or expanding away from the tube. After many months of thermal cycling while in the apparatus and some instances of rough handling, the coil was found to be still quite solidly cemented in position. Commonly, about 6 mA is used, supplying a 12-mG magnetic field. A small correction (about 0.1%) is inserted when calculating the field amplitude from the current to account for the thermal expansion of the entire vapor tube when it is at running temperature.

D. Light detection

Elimination of the thermal oven light from the optical path is easily achieved through the use of simple optical elements. The 6-mm-diam, 30-cm steel tubes (blackened inside) extending from the oven ends greatly reduce the detected solid angle for the oven blackbody light. Downstream of the analyzer, the light is spectrally filtered by reflection from a diffraction grating (600 lines/mm blazed for 1-μm light). A long optical path including a converging mirror and pinhole spatially filters out nearly all of the diverging thermal light before the detector.

The light detector uses a Mitsubishi PD7006 $In_xGa_{1-x}As$ p-i-n diode. This diode has a quantum efficiency of greater than 90%. The detector circuit uses a 50-MΩ feedback resistor, unbiased for lower noise, with a ×100 preamplification stage. The choice of the magnitude of the feedback resistor is constrained by its effects on the bandwidth of the detector and on the Johnson noise. With this feedback resistance and angle modulation of 10^{-3} rad, Johnson noise and shot noise contributions to the angle noise are about equal when 60% of the incident light is absorbed by the atoms. In the higher transmission wings of the angle signal the noise is dominated by vibrations and air currents. The $2\,\omega$ component of the signal sets the upper end of the frequency response bandwidth of the detector circuit, necessitating an extremely low input capacitance (a few pF). A low-noise field-effect transistor cascode preamplifier was built, based on an existing design [16]. A notch filter is used before the 1ω phase-sensitive detector (PSD) to remove the larger 2ω component, increasing the PSD sensitivity to the 1ω signal.

VI. DATA ACQUISITION

Optical rotation measurements are made by repeatedly stepping the laser frequency up and down across the $M1$

transition. Three traces are recorded simultaneously: the Fabry-Pérot cavity transmission, the oven tube transmission, and the oven tube angle times the transmission. A single sweep takes roughly 5 s. After data are taken on an upsweep and a downsweep, the laser continues to ramp, but the oven is turned on for the next up- and downsweep to maintain the lead sample temperature and no data are taken. After several sweeps of data are averaged on either the lead or dummy tube, the tubes are rotated to interchange them, the acquisition program pauses again to allow for vibration damping, and then several sweeps are recorded on the other tube. The matched lead and dummy tube data constitute a single data cycle; several such cycles are taken consecutively, alternating whether the lead or dummy tube is first. During the lead-tube half cycle one or two sweeps are taken with a known applied magnetic field and averaged separately to provide lead Faraday rotation data for calibrating the rotation angle. The rest of the sweeps constitute the PNC data and are taken with the magnetic field approximately canceled out on the lead tube. The residual field is typically of order 0.1 mG, resulting in residual Faraday rotation in the parity data of about 1 μrad, and this field is reset after each run. Transmission data taken on the dummy tube show no atomic absorption, but instead record the effects of the laser power and optical elements on the system sensitivity as a function of laser frequency. A single data cycle commonly takes 10 min and a data run consists of 4–8 consecutive cycles.

Between data runs the optics are readjusted to vary the shape of the background rotations. Many of the run parameters and operating conditions are also changed to allow for later systematic analysis. These include laser sweep and cycle timing parameters, the buffer gas pressure, the residual axial magnetic field, and, less frequently, the polarizer-analyzer orientations. After several days of data taking, the data set is complete and a new one begins at a different temperature of the oven to produce a different number of absorption lengths and a different line shape. The entirety of the lead parity data consists of 1422 data cycles taken in seven data sets. The seven data sets provide measurements of the PNC rotation with seven different line shapes and optical depths, ranging from 10 to 65 absorption lengths. The magnitude of the parity rotation is linear in the number of absorption lengths, so the signal size is significantly larger in the highest absorption data. It is necessary to take much more data at the lower optical depths to obtain comparable sensitivity.

VII. DATA ANALYSIS

Each individual data cycle consists of upsweep (increasing frequency) and downsweep versions of six raw data traces, with typically 200 data points each (and two traces of Fabry-Pérot transmission data). A significant amount of information is contained in the atomic line shapes. Extraction of many line-shape parameters is used both for the final fit to the magnitude of the parity rotation line shape and for later systematic analysis.

The analysis programs analyze each data cycle separately using a Levenberg-Marquardt algorithm to fit each of the six traces to a many-parameter theoretical function [17]. The fits are, in order, the lead tube Fabry-Pérot cavity transmission trace, the dummy tube Fabry-Pérot cavity transmission trace, the transmission measured during the Faraday sweeps, the Faraday rotation, the transmission measured during the parity sweeps, and the parity data with the background rotation subtracted off. First the upsweep data of the cycle are analyzed and then the downsweep.

The detailed atomic line shapes allowed us many options for the form of the fit algorithm and determination of the fit parameters. To rule out any dependence of our result on the particular fit algorithm, all of the data were fit with more than ten different versions of the fit program, as described below. Further details of the line-shape functions are given in the Appendix.

The first information needed by the fits is the laser frequency as a function of computer bin number. For this, the Fabry-Pérot trace is fit to an Airy function, with a four-term polynomial parametrization of frequency vs computer bin number. Four other fit terms take into account the signal offset, amplitude, amplitude slope, and the cavity finesse.

Next, the transmission data for the lead tube are fit using Eq. (A14). The transmission data taken during the Faraday traces and the parity traces are fit separately. The absorption profile is a convolution of the Gaussian Doppler broadening and the Lorentzian pressure broadening, known as a Voigt profile. Additional convolution to account for the few megahertz laser linewidth was found to be unnecessary. We found numerical integrations of the Voigt profile to precision sufficient for our experiment to be time consuming and inefficient; our fit routine used an analytic expansion that converges rapidly to the Voigt profile and is valid when the Lorentz width is less than the Doppler width. Tests comparing the analytic series expansion of the Voigt profile with a full numerical convolution indicate discrepancies in our analytic algorithm at the level of double-precision roundoff error for all regimes of interest encountered in the lead data. The transmission fit parameters are the absorption length, the Gaussian width, the Lorentz width, an overall dc transmission amplitude, the frequency sweep offset, and the laser off-mode light, all defined explicitly in the Appendix.

In the standard version of the fits, all of the traces but the Fabry-Pérot are weighted according to a semiempirical noise model function that varies across the line shape. This weighting function contains terms for all significant noise sources, including angle noise due to the table vibrations, shot noise in the laser light, and noise due to laser frequency jitter.

Next, the Faraday angle times transmission data are fit using Eq. (A17). In principle, the transmission factor is known from the previous fit. However, the Faraday rotation line shape is also Lorentz and Doppler broadened and in some versions of the fit these linewidth terms are refloated here. All versions of the fit float a frequency axis offset term, a dc angular offset term, and the amplitude of the Faraday rotation angle. This last term can be compared to a theoretical prediction of the rotation due to the known magnetic field and thus constitutes an absolute angle calibration of the apparatus.

The typical quality of these fits can be seen in Fig. 5. Possible systematic effects due to any small fit residuals will be discussed in Section VIII C.

Finally, the PNC data are analyzed using Eq. (A19). The raw parity data contain the sum of the parity rotation, the Faraday rotation due to residual magnetic fields, and the background rotation, all multiplied by the transmission function of the vapor. The first step is to remove the effects of the background angle by subtracting the dummy tube data from the raw PNC data. An example of the background rotation angle subtraction for one data cycle is given in Fig. 6. Note that at line center there is no transmission and therefore no rotation signal. The measured background rotation for this particular data cycle is shown in Fig. 6(b). The dummy tube rotation data must be multiplied by the known transmission envelope for correct subtraction from the raw parity data.

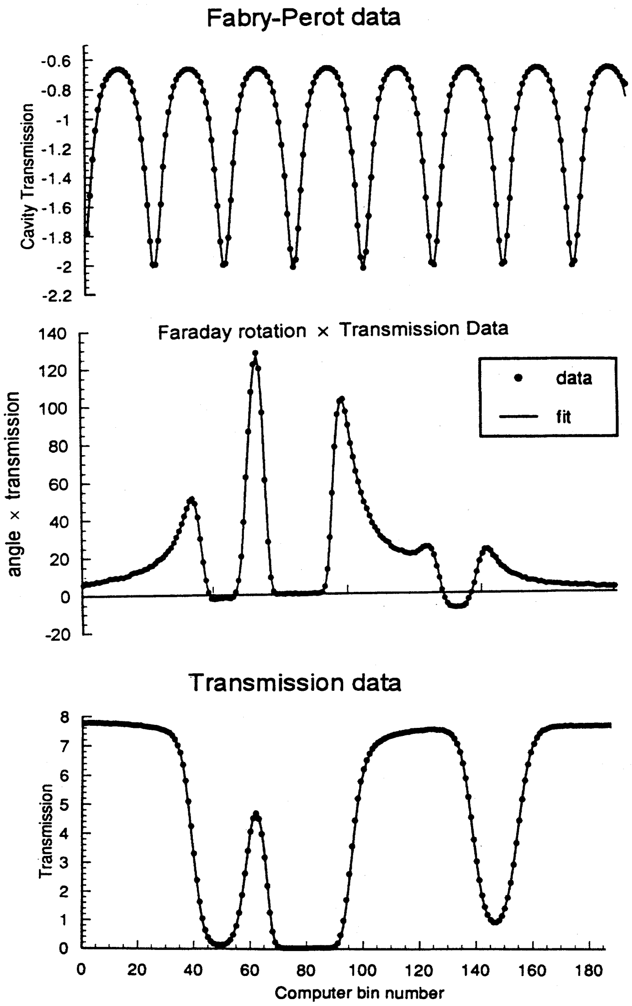

FIG. 5. Fabry-Pérot, Faraday, and transmission rotation data and fits (solid lines) from a single 10-min cycle of a data run at 20.8 absorption lengths.

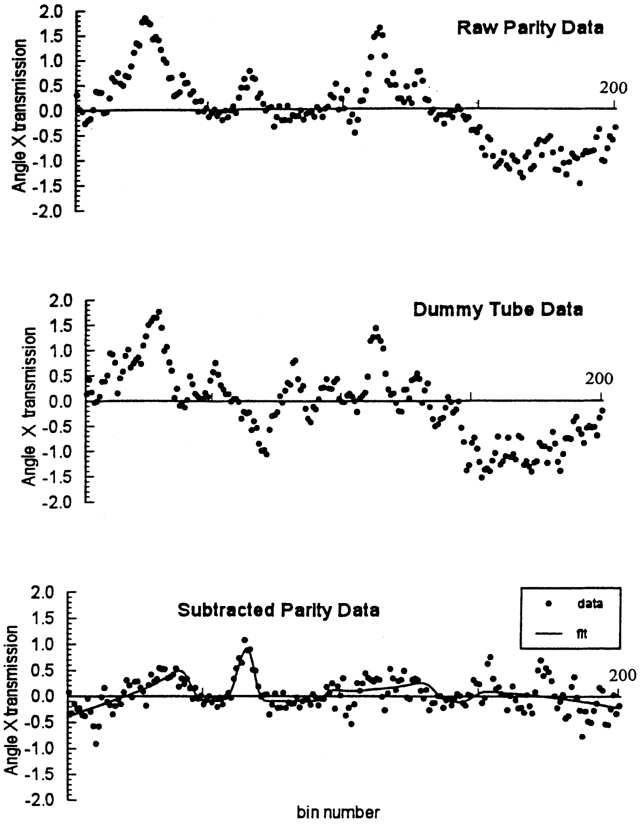

FIG. 6. Background angle subtraction for data cycle 0205b.2. The y-axis units are μ rad. Note that the y axis is expanded for the subtracted parity data trace. The frequency axis spans 7 GHz.

The subtracted data are fit to a term for the amplitude of the residual Faraday rotation, a term for the amplitude of the parity rotation, and a set of one to three terms for a parametrization of $\Delta\phi_{\text{back}}$, the background angle that remains in the data because of imperfect subtraction. The residual Faraday rotation is typically of the same magnitude as the parity rotation, but is readily distinguished from it in the fit because the parity rotation line shape is antisymmetric about each line center, while the Faraday rotation line shape is predominantly symmetric and nearly orthogonal to the parity line shape. The typical quality of these background-subtracted parity fits can be seen in Fig. 6.

The imperfect background subtraction is due in part to drift in the size and shape of the background rotations over the time interval Δt between lead and dummy tube sweeps, allowing a residual angle term $\Delta\phi_{\text{back}}(\nu) = \phi_{\text{back}}(t) - \phi_{\text{back}}(t + \Delta t)$ to remain in the corrected parity trace. Decreasing Δt would result in a reduction of the data-taking duty cycle, since we wait approximately 30 s for the system to settle after rotating the tubes. It is also possible that vibrations caused by rotating the tubes contribute to $\Delta\phi_{\text{back}}(\nu)$. $\Delta\phi_{\text{back}}(\nu)$ can project onto the fitted parity rotation line shape and its varying effects are the major source of scatter in the parity measure-

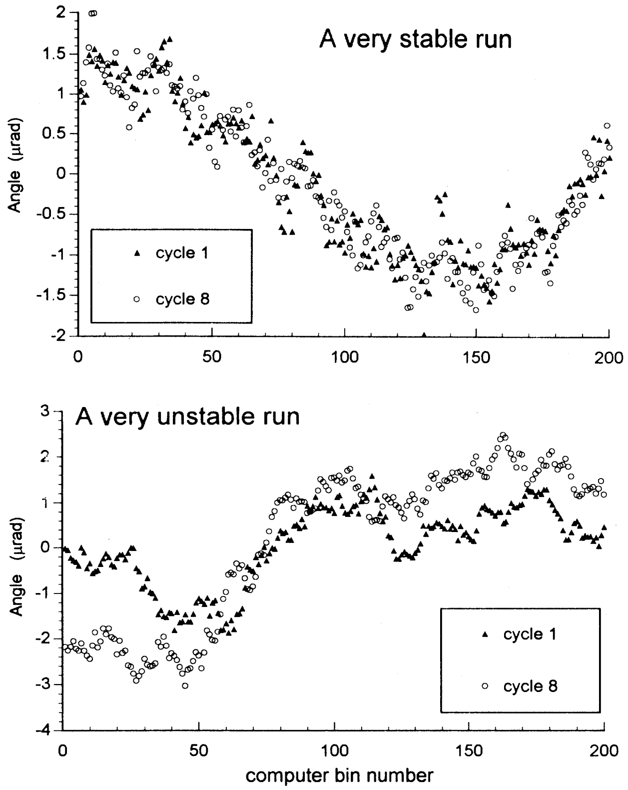

FIG. 7. Dummy tube angle measurements from cycles 1 and 8 of run 0309c, a low drift run, and from cycles 1 and 8 of run 0310f, an extremely high background angle drift run. The time lapse between the first and the eighth cycle of a run is typically 1 h.

ments. Examination of successive dummy tube data half cycles shows the background rotation usually drifts no more than 0.05 μrad, but occasionally becomes unstable with much larger drift. Two examples are shown in Fig. 7. The alternation in time of the order of the dummy and lead tube data reverses the effects of steady drift between data cycles, thus minimizing the effect on the value of $\mathcal{R}$ found for the overall run and enabling an unstable run to contribute useful data.

VIII. ERROR ANALYSIS

The overall uncertainty in $\mathcal{R}$ is caused by statistical fluctuations in the PNC rotation signal and by possible systematic errors associated chiefly with the rotation angle calibration and the transition line shape.

A. Statistical fluctuations

The statistical uncertainty in $\mathcal{R}$ is due partly to detector (Johnson) noise and photon shot noise but mainly to fluctuations in the remaining incorrectly subtracted background pattern in the PNC rotation data. In each data cycle, $\Delta\phi_{\mathbf{back}}(\nu)$ has some projection on the dispersive PNC profile and contributes an error to the fit. $\Delta\phi_{\mathbf{back}}$ contains both pure noise components in the actual angle measured due to table vibrations, as well as the true drift in the background rotation shape over the data cycle time. See Fig. 7. It is sensitive to optical alignment and other conditions and changes from cycle to cycle, leading to a scatter of the values of $\mathcal{R}$. Data were averaged by cycle, by run, and by day to search for evidence of nonstatistical scatter. $\Delta\phi_{\mathbf{back}}$ has some variation slower than the data cycle period, causing the day-to-day scatter of $\mathcal{R}$ to be larger than what the cycle-to-cycle scatter would imply ($\chi^2 \sim 2$). That is, the realignment of the optics performed between runs seemed insufficient to completely randomize the effect of $\Delta\phi_{\mathbf{back}}$ on $\mathcal{R}$. However, we observe no evidence of persistent features in $\Delta\phi_{\mathbf{back}}$ over time scales longer than 1 day: the scatter of $\mathcal{R}$ between data sets agrees with the daily scatter within each group, with $\chi^2 \approx 1$. The daily statistical precision in the value of $\mathcal{R}$ is roughly 3% at 10 optical depths and about 1% at 60 optical depths where the PNC rotation is much larger. We have taken more data at the lower optical depths to give them statistical power comparable to that of the higher depths.

The final statistical error in the data comes from the scatter among the statistically independent data set averages of $\mathcal{R}$. The central value for $\mathcal{R}$ is found by a summation over the values found in the separate data sets, with a 1% error added in quadrature with the errors of the first two data sets. For these data sets, the Faraday coil current was monitored via a voltage over a resistor. This measurement was found to be unstable at the 1% level, leading to a corresponding uncertainty in the Faraday calibration magnetic field. For the remaining data sets, the current was directly measured.

B. Calibration

Two different methods of absolute angle calibration were used for these data. The first method used a mechanical rotation and the second used the Faraday rotation of the lead atoms.

The mechanical calibration was found to be less reliable. This approach required several stages. First, the physical rotation of the polarizer mounts is calibrated by reflecting a laser beam from a mirror on the mount. Motion of the beam spot 10 m away was monitored to give the absolute angle of rotation imparted to the polarizer by a micrometer handle on the mount. With this step completed, the optical rotation of the Faraday glass (which is also used for the modulation) may be calibrated as a function of dc voltage to its coil compared to the angle imparted by the polarizer mount. Finally, before each data cycle, the system sensitivity (output signal) is calibrated to a known rotation (i.e., a known dc voltage sent to the Faraday glass coil). This stepwise calibration method was found to be uncertain at the 1% level due to polarizer imperfections and laser beam divergence. The estimated error is based on observed variations in the Faraday glass calibration as the optical path is changed (particularly after disassembly and reassembly of the oven) and on differences in results using Nicol- and Glan-Thompson-type calcite polarizers. In addition, great care must be taken to properly account for the effects of the oven windows on the calibration and on rotations caused by the atoms in the sample as described in Sec. V C.

Using the atomic Faraday calibration, $\mathcal{R}$ is found from the ratio between the PNC fit and Faraday fit amplitudes. In this method, uncertainties stem from either the magnetic field determination or errors in the fitting procedure for the Faraday rotation line shapes and not from the optical configuration of the apparatus.

The accuracy of the calculated magnetic-field depends on the characteristics of the Faraday magnetic-field coil. As mentioned, the coil was wound onto the lead sample tube using a lathe and is precisely positioned. The coils are glued down to the tube at four places in each turn and a correction factor to the magnetic-field (of about 0.1%) is included to account for expansion of the Mullite tube with temperature. The magnetic-field uncertainty is determined by uncertainties in the number of turns per unit length and in the current. The current was measured directly with an ammeter (to 0.1% accuracy) during all but the first two data sets. As a check of the coil spacing, the number of turns was counted to be 180 turns over 114.5±0.3 cm, giving 3.993±0.010 turns/in., agreeing with a fractional uncertainty of 0.3%. Since the magnetic field needed is the integrated field along the optical path in the lead vapor, the field calibration is not sensitive to local variations of the coil spacing except in conjunction with axial variations in lead density. In the limit that the spacing between turns approaches the circumference of the coil, the magnetic field off axis will differ from its nominal value. This could produce a systematic effect if the laser beam is not on the axis. For our geometry, however, the possible magnitude of this effect is too small to be relevant. The field within a solenoid is also very insensitive to image currents formed by the magnetic shielding. Overall, we compute an uncertainty of 0.5% in determination of the magnetic field. As an independent check, a fluxgate magnetometer probe was inserted down the tube *in situ* and the magnetic field directly measured. The accuracy of this measurement was limited to 0.7% by the calibration of the probe to a reference coil. This calibration agreed with the calculated value, finding an effective turns per inch of 4.016±0.029.

The atomic Faraday calibration method offers further advantages. It avoids the aforementioned uncertainty in calibration due to beam realignment and optical elements, which cancel out when comparing the Faraday and PNC rotations of the same atoms. In addition, errors in the line-shape parameters will largely cancel in determining $\mathcal{R}$, since $\mathcal{R}$ is found from the ratio between the PNC fit and Faraday fit amplitudes. As a simple example, consider the effect of an error in the determination of the absorption depth from the transmission fits. The number of absorption lengths is an amplitude factor for both the Faraday and the parity rotation. In the Faraday fit the calibration term would adjust to compensate and in the final ratio the value for $\mathcal{R}$ would be corrected. Agreement between the more uncertain mechanical calibration and the atomic calibration serves as an important check that the optical depth of the sample and other important fit parameters have been properly extracted from the fitting routines, and that our line-shape model is substantially correct. The angle calibration uncertainties other than magnetic-field calibration are most naturally included as part of the line-shape systematic error in the analysis summarized in the following subsection.

C. Atomic line-shape model

Imprecisely modeled atomic line shapes could lead to fitting errors and possible systematic errors in $\mathcal{R}$. Line-shape errors could be caused by systematic deviations of the laser frequency sweep from the four-term polynomial fit to the bin number, unaccounted laser width or spectral properties of off-mode light, deviations of the oven temperature profile from square (uniformity throughout the heated region and sharp cutoffs at the cold ends), errors in the atomic parameters (line positions, isotopic abundances), nonlinearities in the detection electronics, drifting magnetic fields, transverse magnetic fields, a non-Maxwellian velocity profile of the vapor, complicated non-Lorentzian collision processes, or background molecular absorption.

For the anticipated sources of line-shape error from a known mechanism, upper limits were placed on the possible projection of the effect onto the measurement of the PNC magnitude by studies with simulated line shapes or attempted extraction of appropriate extra parameters. All of these limits were negligibly small. It is also necessary to look for signs of line-shape error in a general fashion, without presuming a particular mechanism. One important way to do this is to examine the measured line shapes closely by combining groups of data and their fits, thus reducing statistical noise and highlighting possible line-shape errors. The groups are combined by binning the data according to laser frequency. All of these binned groups of data did indeed show small non-statistical residuals. The residuals found for the binned parity data are dominated by the net effect of imperfect background subtraction and appear randomly distributed across the line. The transmission and Faraday binned residuals, on the other hand, are well resolved and give information about possible line-shape errors.

Considerable effort was put into uncovering the source of these residuals. All of the data were refit with more than ten different versions of the fit program. The detailed atomic line shapes of the data contain much information and allow us many options for the form of the fit algorithm and determination of the fit parameters. Since all the fitting algorithms left some residuals, with rms size below the 1% level when averaged across the absorption profile, it was necessary to rule out any dependence of our result on any particular fit algorithm. Results of several of the fit variations are shown in Table I.

Here we describe the fit versions in order of their appearance in the table. The standard1 version of the fit parametrized $\Delta\phi_{\text{back}}$ as a constant plus a term linear in

TABLE I. Results from several different versions of the fit program. Each central value and χ^2 are calculated as explained in Sec. VIII A.

Version of fit	$\mathcal{R}$	χ^2
standard1	-9.87(4)	0.9
ϕ_{drift} quadratic parameterization	-9.85(4)	1.1
alteration of atomic parameters		
isotopic abundances	-9.86(3)	0.5
isotope shifts	-9.89(5)	1.3
fixed linewidths in Faraday	-9.86(4)	1.2
transmission fit terms for sweep width	-9.83(5)	1.2
spin-dependent term floated	-9.88(5)	1.4
alteration of the weighting function		
unweighted fits	-9.83(6)	2.1
frequency jitter of 0 MHz	-9.72(9)	4.6
frequency jitter of 1 MHz	-9.83(5)	1.3
frequency jitter of 300 MHz	-9.88(5)	1.1
standard2	-9.88(5)	1.3

ν. Using only a constant term was found to greatly increase the χ^2 for the fits at the lower absorption lengths since the relative signal size is much smaller and imperfect background subtraction would have a larger effect on $\mathcal{R}$. Another version parametrized $\Delta\phi_{\text{back}}$ as a quadratic function. Because there is substantial isotopic variability in samples of "natural" lead, the isotopic composition of the sample could have led to incorrectly parametrized atomic line shapes. The lead isotopic abundances in the sample were directly measured with a mass spectrometer [18], but we used fits to all of our transmission data as an alternative attempt to measure the abundances. The values found were not very accurate, but to check for sensitivity of $\mathcal{R}$ to the abundances, all of the data were refit with these values as shown in the table. Similarly, the isotope shifts are well known [19], but we checked the effects of fitting the data with different values found in the same way. The "fixed linewidths in Faraday" version held the Gaussian and Lorentz widths fixed to their transmission fit values during the Faraday fit. The "transmission fit terms" version floats the quadratic and cubic frequency sweep terms in the transmission fit and uses the new values (instead of those from the Fabry-Pérot fits) in the Faraday and parity fits. The "spin-dependent term" fits float a spin-dependent PNC term in the parity fit. Other versions varied the weighting function of the data. We feel this to be a particularly important test since different fits emphasized different portions of the line shape, where residuals in the fits were significantly different. The "frequency jitter" term of the weighting function accounted for the effects of any possible laser frequency jitter. This term significantly de-emphasizes data near steep slopes of angle or transmission versus frequency, causing the fit to be sensitive only to the wings of the line shape. In the "Standard1" version of the fit, this term is set equal to 15 MHz, based on measurements of the laser frequency. Finally, "Standard2" differed by both a quadratic parametrization of $\Delta\phi_{\text{back}}$ and a frequency jitter of 4 MHz.

The scatter among the different fits is consistent with the statistical errors of systematic effects. While we have not found the source of the residuals, the variety of residual shapes created without significantly altering the final value of $\mathcal{R}$ outside the statistical error bars indicates that any systematic effect associated with the residuals is small. We use the spread in values of $\mathcal{R}$ in Table I to place a bound on the error due to an improper line-shape function, leading to an uncertainty of 0.7% from this source.

D. Correlations

The final lead data consisted of 1422 data cycles in 7 data sets. The 16 separate line-shape channels of each data cycle were characterized by 18 operating condition variables and about 82 fit parameters (plus errors), depending on the version of the fit. Tabulation of the data extracted 45 parameters for correlations analysis. The software used for correlations analysis allowed correlations values to be extracted for any two parameters, cuts on the data to be made, and creation of histograms and scatter plots.

The two most notable examples of potential correlations involved the residual magnetic field and the frequency sweep direction. The residual magnetic field on the sample causes a residual Faraday rotation and for this parameter we found the most clearly resolved possible correlation of the fit parameters investigated. A scatter plot of $\mathcal{R}$ vs the residual magnetic field was fit to a line and produced a slope with a nominal accuracy of 3.7σ. While this slope is well resolved, it is highly sensitive to outliers, so the accuracy is suspect. Using this slope to extrapolate $\mathcal{R}$ to a residual magnetic field of zero adjusts its value by 0.2%, well within the statistical error of $\mathcal{R}$.

The difference between the value of $\mathcal{R}$ found in the upsweep data and the downsweep data was found to be $\Delta\mathcal{R} = 0.15(4)$ in the weighted fits and $\Delta\mathcal{R} = -0.08(5)$ in the unweighted fits. Residual effects of the sweep direction are expected to reverse between the upsweeps and the downsweeps. To the extent that this is not true, a systematic error can be introduced by $\Delta\mathcal{R}$. Yet it is seen that these different versions of the fit that vary $\Delta\mathcal{R}$ so significantly only vary $\mathcal{R}$ itself by 0.2%, well within the statistical error of the sample.

Figure 8 shows the values of $\mathcal{R}$ for the seven data sets plotted vs the number of absorption lengths. The results provide a powerful general systematic check. As can be seen from Fig. 9, the parity rotation line shape varies significantly with absorption length. This variation causes the data sets to have different sensitivities to various possible systematic effects. For example, data taken at lower absorption lengths have a smaller signal size and are therefore more sensitive to the effects of the background rotations. These data can, however, measure the rotation closer to line center. Data taken at higher temperatures have a larger parity rotation amplitude, but are more likely to be affected by molecular absorptions or a non-Maxwellian atomic velocity profile. As can be seen in Fig. 8, the seven data sets are in excellent agreement within their statistical error bars.

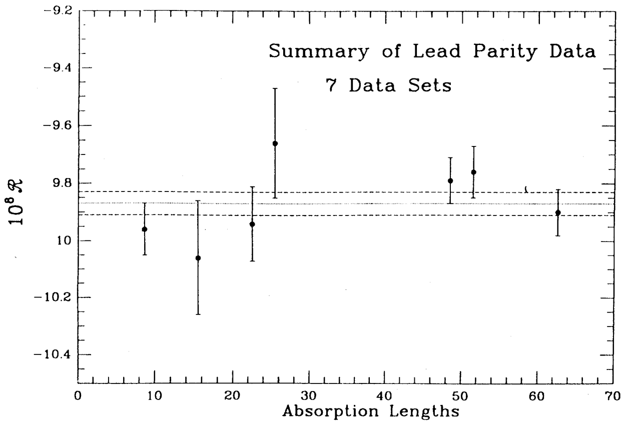

FIG. 8. Value of $\mathcal{R}$ plotted versus absorption length for the seven data sets. The error bars show statistical uncertainties only. The error bar for each data set is corrected for its χ^2 to reflect the effects of the scatter due to background drifting. The χ^2 for the weighted average of the seven measurements of $\mathcal{R}$ by the data sets is 0.9. The horizontal dashed lines represent the $\pm 1\sigma$ uncertainty of the combined weighted average.

None of the correlations indicate the need for extrapolating $\mathcal{R}$ beyond the statistical error. The maximum extrapolation indicated by combining all the correlations studied leads to a systematic error associated with correlations of 0.7%. Adding the three types of systematic errors (magnetic-field calibration, line-shape, and correlation) in quadrature, the overall systematic error is found to be 1.1%.

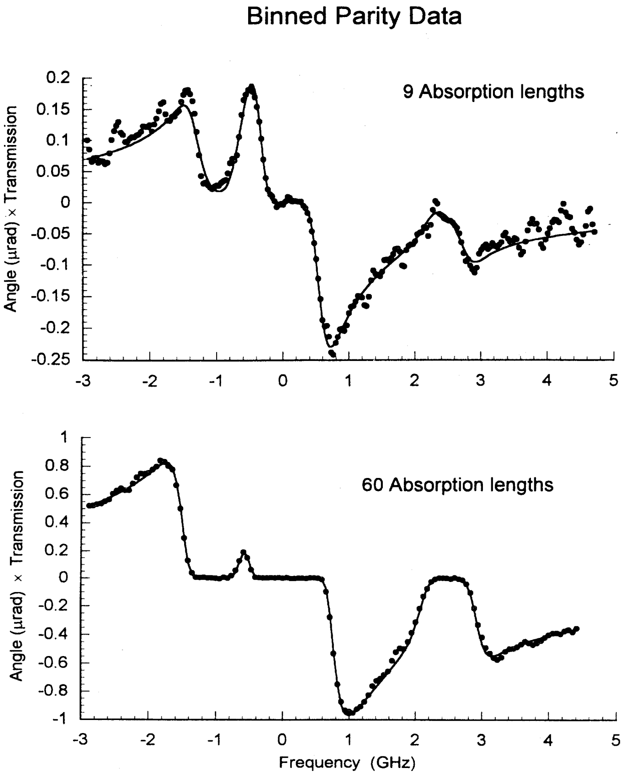

FIG. 9. Binned parity rotation data from the data sets at 20 and 60 absorption lengths, representing 100 and 40 h of data acquisition, respectively. The residual Faraday rotation shape has been subtracted.

IX. RESULT AND DISCUSSION

The final central value for $\mathcal{R}$ is computed from the average of the central values of $\mathcal{R}$ found by the seven main versions of the analysis program. The five fit versions not included in this average are those intended as systematic checks only and not believed to accurately represent the line shape, the versions with altered atomic parameters, and frequency jitter terms of 0, 1, and 300 MHz. The final value of the PNC optical rotation in lead, normalized to ^{208}Pb is

$$\mathcal{R} = (-9.87 \pm 0.04 \pm 0.11) \times 10^{-8},$$

where the first error is statistical and the second is systematic. This is the highest-precision measurement of atomic parity nonconservation to date.

As a consequence of the complicated electronic structure in lead, the best calculation to date of PNC is uncertain at the 8% level, with the result $\mathcal{R} = -10.2 \pm 0.8$ [20]. No improved calculation of the atomic theory for lead is expected in the near future. The uncertainty of the theory presently limits the ability to extract precise values or limits for electroweak parameters from this experiment, but one can extract a value for the isospin-conserving electroweak parameter [2]

$$S = -3 \pm 8.$$

An improved calculation would have obvious applicability.

A nuclear spin-dependent PNC effect in lead ($\mathcal{R}_{\rm SD}$), induced by the C_2 terms in Eq. (1) and by electronic interaction with a nuclear anapole moment, would appear as dispersive optical rotation of opposite sign on the two hyperfine components of the odd isotope ^{207}Pb. Such effects are lower by a factor of Q_w relative to the spin-independent rotation and theoretical predictions for this effect in lead are particularly small [21] relative to other heavy atoms on which PNC experiments can be performed. By fitting explicitly for the spin-dependent line shape we are able to set the upper limit $\mathcal{R}_{\rm SD}/\mathcal{R} < 0.02$ (95% confidence), where here $\mathcal{R}$ refers to the spin-independent rotation of the ^{207}Pb, $F = 1/2 \rightarrow 3/2$ hyperfine line.

The most immediate application of the improved experimental technique described here is, as mentioned in the Introduction, the measurement of PNC in thallium at approximately the same wavelength [7]. As a long-range goal, a method for removing the uncertainties due to atomic structure would be to take ratios of PNC measurements on single isotopes, thereby canceling the structure factor. Lead is a good candidate for such measurements, as there are several stable isotopes. The major difficulty would be the small magnitude of the measured quantity, which is reduced by a factor of $\Delta N/N$, requiring significant further improvement of the experimental technique. If the measurements were successful, the effect of nuclear structure would eventually have to be taken into account. The present uncertainties in the neutron distributions are estimated to contribute a fractional uncertainty of 0.5% for measurements of PNC ratios in lead [11]. An interesting feature of PNC ratios among isotopes is that the unique dependence of the measurement on S, the parameter of isospin-conserving extensions to the standard model, is lost: the ratio is sensitive to the same linear combination of radiative corrections to the standard model as that of the high-energy measurements of $\sin^2\theta_w$.

ACKNOWLEDGMENTS

We would like to thank J.M. Reeves and T.D. Wolfenden for assistance at earlier stages of the experiment and B. Nelson for determining the isotopic composition of our sample. This work is supported by National Science Foundation Grant No. PHY-9206408.

APPENDIX A: THEORETICAL LINE SHAPES AND FITTING FUNCTIONS

The atomic absorption line shapes we observe exhibit both collisional and Doppler broadening. For the collisional broadening we assume a Lorentzian shape

$$\mathcal{L}(\nu-\nu_0)=\frac{\Lambda/2}{4\pi^2(\nu-\nu_0)^2+\Lambda^2/4}, \tag{A1}$$

where Λ is the Lorentz half-width, usually less than 20 MHz in our experiment. The dispersion line shape corresponding to the Lorentz absorption shape in Eq. (A1) is

$$\mathcal{D}(\nu-\nu_0)=\frac{\nu-\nu_0}{2\pi(\nu-\nu_0)^2+\Lambda^2/8\pi}. \tag{A2}$$

This is admittedly an approximation and neglects more complicated collisional processes, but such effects are small and are treated as possible systematic error sources in the main text. The Doppler effect of the motion of the atoms on the laser frequency in the rest frame of the atoms requires an integration over the velocity distribution. The distribution of the velocities of the atoms in the oven is Maxwellian $\mathcal{M}(v)$,

$$\mathcal{M}(v)\,dv=\frac{1}{\sqrt{\pi}v_0}\exp\left(-v^2/v_0^2\right)\,dv, \tag{A3}$$

where

$$v_0=\sqrt{2kT/M} \tag{A4}$$

and M is the atomic mass. The Doppler linewidth

$$\Gamma=\frac{2\pi\nu_0v_0}{c} \tag{A5}$$

gives the half-width at $1/e$ maximum (typically $\cong$ 250 MHz) in the limit that the Lorentz width is negligible. The atomic mass dependence causes the Doppler broadening for ^{204}Pb to be about 1% larger than that for ^{208}Pb.

The convolved line shapes are

$$\mathcal{D}'(\nu)=\int\mathcal{D}\left(\nu-\nu_0\left(1-\frac{v}{c}\right)\right)\mathcal{M}(v)\,dv, \tag{A6}$$

$$\mathcal{L}'(\nu)=\int\mathcal{L}\left(\nu-\nu_0\left(1-\frac{v}{c}\right)\right)\mathcal{M}(v)\,dv. \tag{A7}$$

The convolution of a Lorentzian and a Gaussian profile is known as a Voigt profile. No analytic solution exists for either integral. For our data fits, we used fast analytic expansions that are valid when the Lorentz width is smaller than the Gaussian width.

The absorptivity of the vapor is the sum of the absorptivities of the four isotopes, with two separate lines for ^{207}Pb. The relative abundances (including a factor for the hyperfine line strengths) are given by S_n. The optical depth is

$$\mathcal{A}(\nu)=\beta\sum_n S_n\mathcal{L}'(\nu-\nu_n) \tag{A8}$$

and the transmission is

$$\tau(\nu)=e^{-\mathcal{A}}. \tag{A9}$$

The number of absorption lengths β is proportional to the number of atoms in the vapor (a uniform vapor density times a path length is assumed here—vapor density variations can be included by numerically integrating a radiative transfer equation). The overall scale factor in S_n is commonly adjusted to make $\beta=1$ when the transmission at the peak of the resonance is e^{-1}.

The PNC rotation is introduced and discussed in Sec. III. Equation (9) may be written in terms of the notation above as

$$\phi_{\text{parity}}=\mathcal{R}\phi_P=\beta\sum_n\mathcal{R}_nS_n\mathcal{D}'(\nu-\nu_n). \tag{A10}$$

There are two components to the Faraday rotation. The larger is due to the splitting of the Zeeman sublevels by the magnetic field. The transition line centers are shifted a small amount ϵ so that the differential index of refraction is $n_+-n_-=n(\nu+\epsilon)-n(\nu-\epsilon)\to2\epsilon\frac{dn}{d\nu}$. The Faraday rotation, then, varies as the frequency derivative of the dispersion curve

$$\frac{d\mathcal{D}}{d\nu}=\frac{\Lambda^2/8\pi-2\pi(\nu-\nu_0)^2}{\left[2\pi(\nu-\nu_0)^2+\Lambda^2/8\pi\right]^2}. \tag{A11}$$

This is also Doppler broadened

$$\mathcal{F}(\nu-\nu_0)=\int_{-\infty}^{\infty}\mathcal{M}(v)\,\frac{d\mathcal{D}(v)}{d\nu}\,dv. \tag{A12}$$

A much smaller component of the Faraday rotation is antisymmetric across the line center. The magnetic field mixes pairs of hyperfine states of a given J proportionally to m_F. This mixing causes a different transition amplitude for different Δm_F values, leading to a different amplitude of the refractive index for the two circular polarizations. The net optical rotation due to these two contributions caused by an axial magnetic field $\mathbf{B}\cdot\mathbf{k}$ is thus

$$\begin{aligned}\phi_{\rm Faraday} &= B\phi_F \\ &= \beta(\mathbf{B}\cdot\mathbf{k})\sum_n g_n S_n\left[\mathcal{F}(\nu-\nu_n)+\epsilon_n\mathcal{D}'(\nu-\nu_n)\right],\end{aligned} \tag{A13}$$

where the g_n factors are of order 1 MHz/G and ϵ_n is nonzero only for ^{207}Pb.

Now consider the expected line shapes as they are measured in the data. In the following equations the measured quantities, written in uppercase german font, are used to determine the various fit parameters. The dummy tube transmission data are used to measure the power of the laser light as a function of frequency, giving $\mathfrak{T}_{\rm dummy}(i_{\rm bin}) = a(\nu) + I_{\rm off}$. $I_{\rm off}$ is the laser off-mode light or, indistinguishably, any offset in the 2ω PSD measuring the transmission. In the transmission fits, the value of $I_{\rm off}$ is allowed to vary as an offset term. It is then held fixed for the angle fits. In all of the fits, the laser power amplitude is given by $a(\nu) = \mathfrak{T}_{\rm dummy}(i_{\rm bin}) - I_{\rm off}$.

The lead tube transmission data are

$$\mathfrak{T}(i_{\rm bin}) = a(\nu)\,\tau(\nu) + I_{\rm off}. \tag{A14}$$

The Faraday rotation data are the product of the rotation angle and the transmission

$$\begin{aligned}\mathfrak{F} = a(\nu)\tau(\nu)&\left[(B_{\rm app}+B_{\rm resid})\phi_F + \mathcal{R}\phi_P + \phi_{{\rm back},F}\right]\\ &+ I_{\rm off}\phi_{\rm off}.\end{aligned} \tag{A15}$$

The measured line shape contains not only the rotation due to the applied magnetic field $B_{\rm app}$ but also the rotation due to the residual magnetic field $B_{\rm resid}$ and the PNC rotation $\phi_{\rm parity}$. The angle of the off-mode light $\phi_{\rm off}$ is assumed to be independent of frequency.

The measured parity data signal is

$$\begin{aligned}\mathfrak{P} = a(\nu)\tau(\nu)&\left[B_{\rm resid}\phi_F(\nu) + \mathcal{R}\phi_P(\nu) + \phi_{\rm back}(\nu)\right]\\ &+ I_{\rm off}\phi_{\rm off}.\end{aligned} \tag{A16}$$

Since the Faraday sweeps are taken just before and after the parity data sweeps, during the same half cycle, all of their parameters (except for $\phi_{\rm Faraday}$) should be the same. Subtracting the parity data from the Faraday data leaves simply

$$\mathfrak{F} - \mathfrak{P} = a(\nu)\tau(\nu)\left[B_{\rm app}\phi_F + \phi_{\rm drift}\right]. \tag{A17}$$

The angle drift between the Faraday sweeps and the parity sweeps is accounted for by $\phi_{\rm drift}$. Since there is so little time between them, $\phi_{\rm drift}$ is quite adequately fit by a dc term. In the fits, a calibration factor C_F on ϕ_F is allowed to vary.

The parity data are corrected for the background angle by subtracting the dummy data. The measured dummy tube angle is

$$\mathfrak{D} = a(\nu)\phi_{{\rm back},D} + I_{\rm off}\phi_{\rm off}. \tag{A18}$$

The dummy data need to be multiplied by the transmission envelope (as calculated from the lead tube transmission fit values) before subtraction from the parity angle data. This gives us

$$\begin{aligned}\mathfrak{P} - \tau(\nu)\mathfrak{D} = a(\nu)t(\nu)&\left[\mathcal{R}\phi_P + B_{\rm resid}\phi_F + \Delta\phi_{\rm back}\right]\\ &+ \left[1 - t(\nu)\right] I_{\rm off}\phi_{\rm off}.\end{aligned} \tag{A19}$$

---

[1] M.A. Bouchiat and C.C. Bouchiat, Phys. Lett. **48B**, 111 (1974).

[2] M.E. Peskin and T. Takeuchi, Phys. Rev. D **46**, 381 (1992).

[3] D.N. Stacey, in *Atomic Physics 13*, edited by H. Walther, T.W. Hänsch, and B. Neizert (AIP, New York, 1993), p. 46.

[4] S.A. Blundell, W.R. Johnson, and J. Sapirstein, Phys. Rev. Lett. **65**, 1411 (1990).

[5] M.C. Noecker, B.P. Masterson, and C.E. Wieman, Phys. Rev. Lett. **61**, 310 (1988).

[6] D.M. Meekhof, P. Vetter, P.K. Majumder, S.K. Lamoreaux, and E.N. Fortson, Phys. Rev Lett **71**, 3442 (1993).

[7] P.A. Vetter, D.M. Meekhof, P.K. Majumder, S.K. Lamoreaux, and E.N. Fortson, Phys. Rev. Lett. **74**, 2658 (1995); N.H. Edwards, S.J. Phipp, P.E.G. Baird, and S. Nakayama, *ibid.* **74**, 2654 (1995).

[8] V.A. Dzuba, V.V. Flambaum, P.G. Silvestrov, and O.P. Sushkov, J. Phys. B **20**, 3297 (1987).

[9] W.R. Johnson, J. Sapirstein, and Z.W. Liu (private communication); A.M. Martenson-Pendrill (private communication).

[10] V.A. Dzuba, V.V. Flambaum, and I.B. Khriplovich, Z. Phys. D **1**, 243 (1986).

[11] E.N. Fortson, Y. Pang, and L. Wilets, Phys. Rev. Lett. **65**, 2857 (1990); S.J. Pollock, E.N. Fortson, and L. Wilets, Phys. Rev. C **46**, 2587 (1992).

[12] E.N. Fortson and L.L. Lewis, Phys. Rep. **113**, 289 (1984).

[13] E.D. Commins and P.H. Bucksbaum, *Weak Interactions of Leptons and Quarks* (Cambridge University Press, New York, 1983).

[14] I.B. Khriplovich, Comments At. Mol. Phys. **23**, 189 (1989), and references therein.

[15] M.G. Boshier, D. Berkeland, E.A. Hinds, and V. Sandoghdar, Opt. Commun. **85**, 355 (1991).

[16] S.R. Jefferts and F.L. Walls, Rev. Sci. Instrum. **60**, 1194 (1989).

[17] W. Press, B. Flannery, S. Teukolsky, and W. Vetterling, *Numerical Recipes: The Art of Scientific Computing* (Cambridge University Press, New York, 1986).

[18] B. Nelson (private communication).

[19] J.M. Reeves and E.N. Fortson, Phys. Rev. A **44**, R1439 (1991).

[20] V.A. Dzuba, V.V. Flambaum, P.G. Silvestrov, and O.P. Sushkov, Europhys. Lett. **7**, 413 (1988).

[21] V.F. Dmitriev, I.B. Khriplovich, and V.B. Telitsin, Nucl. Phys. A **577**, 691 (1994); I.B. Khriplovich, Budker Institute of Nuclear Physics Report No. BINP 94-56, 1994 (unpublished); V.V. Flambaum, I.B. Khriplovich, and O.P. Sushkov, Phys. Lett. **146B**, 367 (1984).